JACS Au
AN OPEN ACCESS JOURNAL OF THE AMERICAN CHEMICAL SOCIETY

pubs.acs.org/jacsau
Article

Flat-Shaped Copper Nanoclusters with Near-Infrared Absorption for Enhanced Photothermal Conversion

Bingzheng Yan,[⊥] Jing Sun,[⊥] Jiahe Liu,[⊥] Lei Li, Hongwen Deng, Qinghua Xu, Song Wang,* and Hui Shen*

Cite This: *JACS Au* 2025, 5, 1884−1893

ABSTRACT: Atomically precise metal nanoclusters have emerged as a prominent area of research in recent years, yet the majority of previous studies have primarily concentrated on gold and silver ones. The challenge of controlling the shape of copper nanoclusters in order to investigate their relationship to properties remains a significant concern in contemporary scientific research. In this study, we successfully achieved shape control of a copper nanocluster with a rare flat oblate structure using a combination of multiple ligands (trifluoroacetic acid, 4-fluorothiophenol, and triphenylphosphine). The resulting nanocluster, with the composition $Cu_{62}(4\text{-F-PhS})_{30}(CF_3COO)_8(PPh_3)_6H_{10}$, features a flat metal core of aspect ratio as high as 2.6, which is stabilized by ligands attached to or bridged onto the flat kernel. Unlike most previously reported copper nanoclusters, Cu_{62} exhibits absorption in the near-infrared range. Density functional theory calculations reveal that the main occurrence of near-infrared transitions takes place at the equatorial radius of the Cu_{62} nanocluster metal core, corresponding to the radial exciton oscillation caused by the confinement of a flattened inner core structure, similar to the plasmon resonance in metal nanoparticles. The unique flattened oblate structure of the nanocluster can also promote the photothermal conversion efficiency (PCE). The temperature of the cluster solution increases from room temperature to around 90 °C in just 10 min, achieving a PCE of approximately 56%. This study not only has the potential to stimulate further research on both the control of copper nanocluster structures and the exploration of their applications but also provides a model system for investigating the relationship between structure and photothermal conversion of copper nanomaterials.

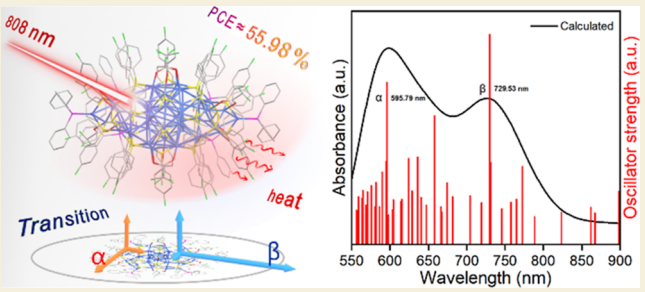

KEYWORDS: *copper, nanocluster, flat shape, crystal structure, photothermal conversion*

1. INTRODUCTION

Ligand-protected, atomically precise metal nanoclusters (NCs) with absolute monodispersion, defined chemical compositions, and clear molecular structures have garnered significant interest in the fields of chemical and material science.[1−3] The unique size of metal NCs, which falls between metal atoms and nanocrystals, combined with their diverse and tunable ligands and kernel structures, give them a wide range of physicochemical properties.[4−6] For instance, metal NCs are considered a novel type of organic−inorganic hybrid nanomaterials in the scientific community studying photothermal conversion.[7−12] One particular aspect of metal NC materials that is of great interest is the strong dependence of their properties on their structures, even at the atomic level.[13−17] This makes them an ideal system for gaining insights into the relationship between structures (such as shape, composition, charge, and interface) and properties (optical, photoluminescent, chiral, and catalytic).[18−22] In terms of shape, metal NCs typically exhibit approximately spherical, block, or rod structures which result from their lower cohesive energy.[23−26] Metal NCs with flat oblate structures are rare, although they have exhibited embryonic properties of interest.[27−30]

Due to their high abundance, diverse structure, and distinct physicochemical properties, copper NCs have been highly pursued in the past several years.[31−34] Pioneering studies conducted by several groups, including Hayton, C.W. Liu, Bakr, Negishi, and Zang, have demonstrated the uniqueness of copper NCs in both fundamental research and application scope.[35−44] For example, copper NCs often contain hydride species in their moieties, which are less common in other noble analogues.[45,46] The high efficiency of copper NCs in catalysis, particularly in organic photocatalysis as recently demonstrated by Bakr et al., suggests a promising future for these materials.[47] However, the synthesis of copper NCs, particularly those with

Received: January 27, 2025
Revised: March 12, 2025
Accepted: March 14, 2025
Published: March 21, 2025

https://doi.org/10.1021/jacsau.5c00099
JACS Au 2025, 5, 1884−1893

special shapes and unique properties, presents greater challenges in current science.[48,49] To the best of our knowledge, there have even been no reports on flat oblate copper NCs with a large kernel. In this context, obtaining copper NCs with a flat oblate geometry is highly desirable, as it provides important insights into shape control, structural characteristics, physicochemical properties, and structure−property relationships of two-dimensional copper nanomaterials.

Herein, we present a new flat oblate cluster of Cu_{62}(4-F-PhS)$_{30}$(CF_3COO)$_8$(PPh_3)$_6H_{10}$ with a metal kernel aspect ratio of 2.6 (referred to as Cu_{62}, 4-F-PhS refers to 4-fluorothiophenol, and PPh_3 denotes triphenylphosphine). The cluster, exhibiting a windmill-shaped core structure and a well-organized organic ligand shell, has been thoroughly characterized by various advanced characterization techniques. Due to its unique sheet-like architecture, the cluster exhibits uncommon absorption in the near-infrared region, which has been confirmed by density functional theoretical (DFT) calculations. Importantly, the cluster demonstrates excellent photothermal conversion properties, achieving a temperature increase from room temperature to approximately 90 °C within 10 min and a high photothermal conversion efficiency (PCE) of up to 55.98% under laser irradiation of 808 nm.

2. RESULTS AND DISCUSSION

The synthesis of Cu_{62} was conducted in a single reaction vessel in the presence of air using the previously developed synthesis prototype (for more details, refer to the Methods section).[50] In this prototype, $Cu(CF_3COO)_2$ was used as the copper precursor, 4-fluorothiophenol as a coprotective ligand, and $(PPh_3)_2CuBH_4$ as the reducing agent. It is important to note that Cu_{62} could not be obtained using other copper salts such as copper nitrate, copper benzoate, and $Cu(MeCN)_4BF_4$ (Figure S1). In the synthesis, $Cu(CF_3COO)_2$ provides not only copper atoms for aggregation but also trifluoroacetate ligands that protect the cluster core. Similarly, the reducing agent $(PPh_3)_2CuBH_4$ plays a crucial role in the synthesis of the clusters, as documented in our previous studies.[51,52] In a typical synthesis, the reduction of $Cu(CF_3COO)_2$ in the presence of 4-fluorothiophenol by $(PPh_3)_2CuBH_4$ in a mixed solvent of dichloromethane and methanol produces a clear dark red solution (Figure S2). The raw product is purified, resulting in the formation of dark red block crystals after 2 weeks (Figure S3). The high purity of the clusters in the raw product was confirmed by the similar visible-near-infrared (UV−vis−NIR) absorption spectra of the crude product and the crystal (Figure S4).

The high-quality crystalline products were initially characterized through single crystal X-ray diffraction (SC-XRD) at 100 K (Figure S5). Analysis of the single-crystal X-ray structure revealed that the Cu_{62} cluster crystallizes in the trigonal space group of $R\bar{3}$ (Table S1), with three independent cluster moieties present in each unit cell (Figure S6). The Cu_{62} cluster is expected to be neutral in charge, as there is no counteranion present in the lattice. The complete structure of the Cu_{62} cluster, viewed from different sides, is shown in Figure 1a. This figure illustrates the stabilization of the Cu_{62} core by a ligand shell consisting of 30 4-F-PhS$^-$, 6 PPh_3, and 8 CF_3COO^- ligands. Notably, the Cu_{62} cluster has a large aspect ratio, with a measured diameter of 28.4813 Å and a height of 19.9376 Å (Figure 1b).

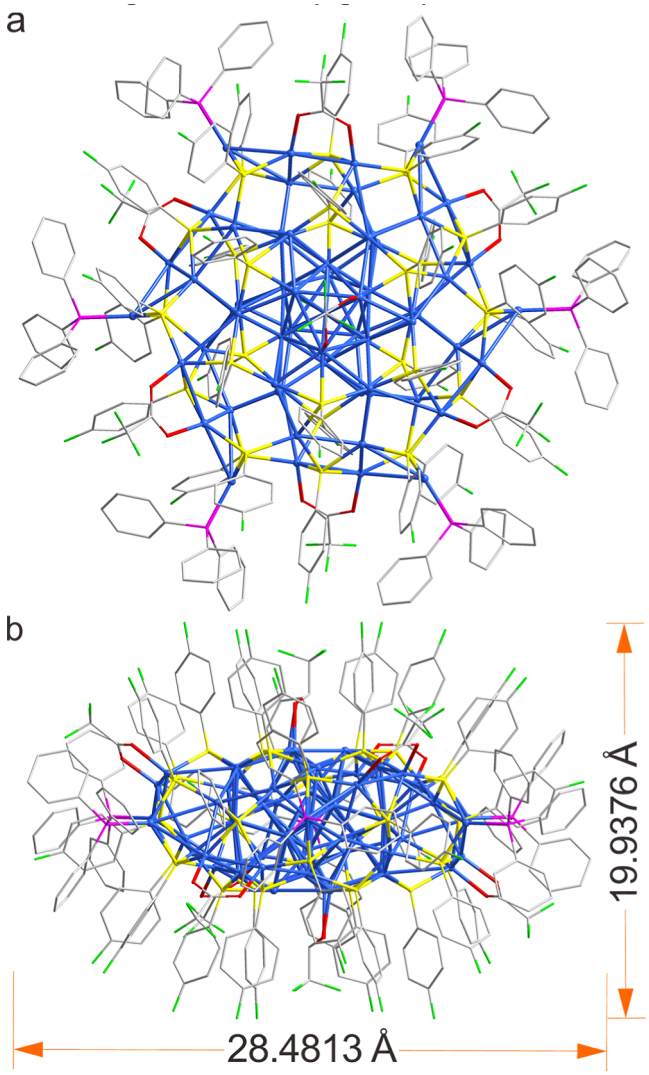

Figure 1. Total structure of the Cu_{62} cluster from the top (a) and side (b) views. Color codes for atoms: light blue, Cu; yellow, S; red, O; bright green, F; pink, P; gray, C. All H atoms are omitted for clarity.

The structural anatomy of Cu_{62} is depicted in Figure 2a. It consists of an internal Cu_8 core, which can be divided into two tetrahedral Cu_4 units with orthotriangular bases. The vertices of the two Cu_4 tetrahedra are connected by a Cu−Cu bond with a length of 2.5839 Å. The value is comparable to that of the Cu_4 tetrahedra, indicating a strong interaction. It is worth noting that the Cu_4 tetrahedra are rotated 60° along the connection axis (pink), and the Cu atoms within each tetrahedron exhibit nearly perfect centrosymmetry. Surrounding the Cu_8 core is a Cu_{12} ring that forms a twisted hexagram. The six vertices of the Cu_{12} ring lie in the same plane, creating a hexagonal plane. However, the vertices of the six concave angles are not in the same plane and the adjacent vertices are staggered on both sides of the hexagonal plane. The Cu_{12} ring encloses the Cu_8 core with an average Cu−Cu bond length of 2.8157 Å (Figure S7), which is larger than that in Cu_4 units. Extending further are 6 Cu_9 units that resemble fan blades. The fan blades, highlighted in different colors, constitute the outermost copper shell and share six copper atoms with the Cu_8 core (Figure S8). The average length of the Cu−Cu bonds for each "fan blade" is 2.859 Å. Overall, the entire Cu_{62} metal framework exhibits a windmill-style geometry with C_3

https://doi.org/10.1021/jacsau.5c00099
JACS Au 2025, 5, 1884−1893

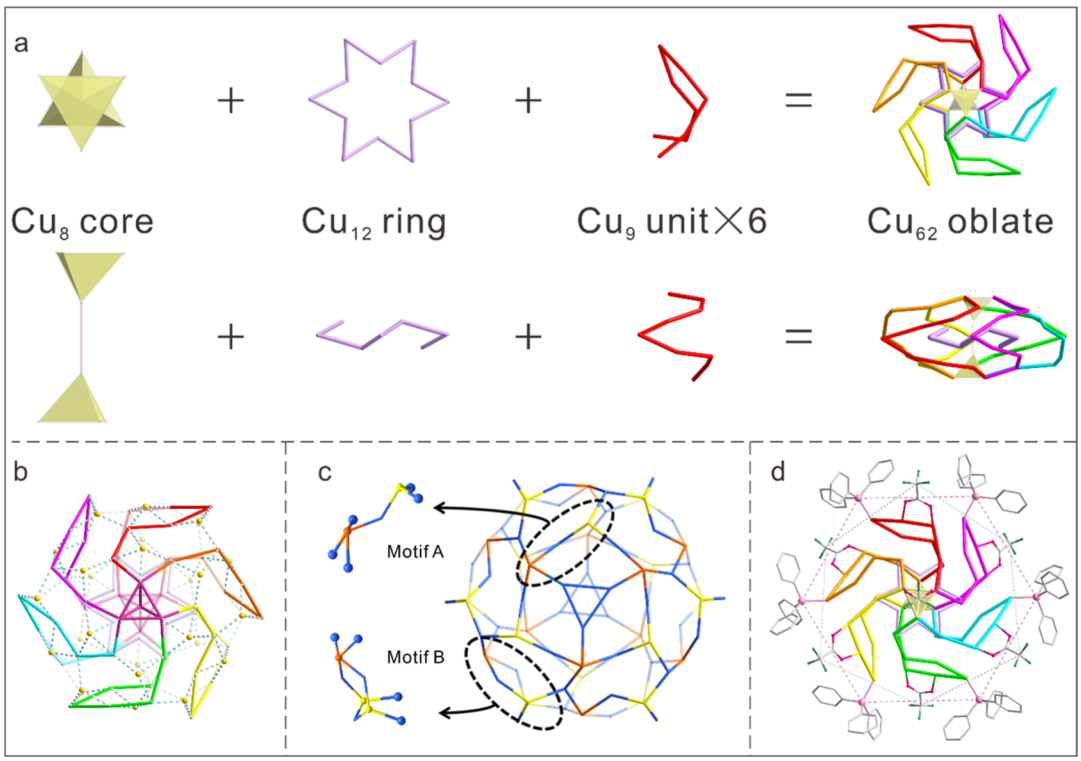

Figure 2. (a) Anatomy of the metal core of Cu_{62}. All atoms are Cu. (b) $Cu_{48}S_{30}$ cage. Color codes for atoms: yellow spheres, S; chromatic windmill, Cu. (c) Coordination modes of thiolate ligands on the surface. Color labels: light blue, Cu; yellow and orange, S. (d) Coordination modes of phosphine ligands and carboxylic acid ligands on the surface. Color codes: chromatic windmill, Cu; rose, P; light red, O; sea green, F; gray, C. All H atoms are omitted for clarity.

symmetry. The equatorial and axial radii of the Cu_{62} kernel are 3.143 and 8.169 Å, respectively, making the aspect ratio of the metal core up to 2.6 (Figure S9).

The 44 ligands coordinate with the surface of the cluster in an organized manner. For instance, the S atoms of thiolate ligands are embedded in the middle of the Cu_{62} fan leaf, creating a $Cu_{48}S_{30}$ cage with the outermost Cu atoms (Figure 2b). As depicted in Figure 2c, the thiolate ligands on the surface exhibit two different coordination modes: μ_3 and μ_4-bridging. When viewed from the *c*-axis, the inner and outer layers of the $Cu_{48}S_{30}$ unit display different motif arrangements due to variations in the Cu−S coordination modes. The inner layer shows a Cu_6S_2 motif (motif A), with one μ_3 and one μ_4-coordinated thiolate ligand directly linked through a Cu atom. Similarly, the outer layer features a Cu_7S_3 motif (motif B), consisting of two μ_3-coordinated S−Cu−S staple structures and a μ_4-coordinated thiolate ligand. The average Cu−S bond lengths are 2.270 and 2.283 Å in Cu_6S_2 and Cu_7S_3, respectively. As shown in Figure 2d, the six phosphine ligands coordinate with six Cu_9 apex atoms, forming a regular hexagon. Such a coordination arrangement of phosphine ligands suggests a similar chemical environment. In accordance with the observation that the six phosphine ligands coordinate to the cluster in a similar chemical environment, ^{31}P nuclear magnetic resonance (NMR) of Cu_{62} in DMF-d_7 shows a single peak at 24.96 ppm (Figure S10). Additionally, the carboxylate ligands are coordinated to the metal core in a C_3 symmetric manner. Out of the 8 carboxylate ligands, 2 are attached to the top and bottom of the Cu_8 core, while the remaining 6 coordinate the shoulder of the Cu_9 fan blade. It is worth noting that the carbon atoms of the trifluoroacetate groups in the toroidal plane combine to form a hexagonal structure that permeates the entire Cu_{62} structure. Energy-dispersive X-ray spectroscopy (EDS) further confirmed the uniform distribution of elements Cu, S, P, O, F, and C in Cu_{62} clusters (Figure S11).

The Cu_{62} cluster appears to be a neutral substance, as no counteranion was observed. Additionally, attempts to confirm Cu_{62} composition using electrospray ionization mass spectrometry (ESI-MS) were unsuccessful, as no corresponding peaks were observed in either negative or positive ion modes. The addition of Cs^+ also did not yield the expected results (Figure S12). However, clear evidence is provided by X-ray photoelectron spectroscopy (XPS). It should be noted that determining the chemical state of copper is challenging due to the overlap in the binding energy of Cu_{2p} from Cu^0 and Cu^+ species. The binding energies of Cu $2p_{3/2}$ in Cu^0 (932.6 eV) and Cu^+ from Cu_2S (932.6 eV) are extremely similar. To gain insight into the oxidation state of Cu, we employed Cu LMM Auger spectroscopy. As shown in Figure S13, the Cu LMM Auger spectrum of the Cu_{62} cluster exhibits a principal peak at 915.8 eV, corresponding to the Cu^+ oxidation state. Additionally, a secondary peak at 918.0 eV, corresponding to the Cu^0 oxidation state, is observed.[53] No satellite signal at 943 eV, indicative of the Cu^{2+} oxidation species, was detected in the Cu_{2p} spectra of Cu_{62} (Figure S14). Therefore, NMR studies were conducted in accordance with the reported strategies to determine the quantity of hydride in the structure.[54,55] Initially, the deuterated analogue $[Cu_{62}(4\text{-}FPhS)_{30}(CF_3COO)_8(PPh_3)_6D_{10}]$ (Cu_{62}-D) was synthesized by using $(PPh_3)_2CuBD_4$ as the reducing agent (Figure S15). The ^1H NMR spectra of Cu_{62} and Cu_{62}-D were carefully compared, revealing that the hydride signals at 8.31 and 2.07 ppm in Cu_{62} were absent in Cu_{62}-D (Figure S16). Subsequently, the number of hydride atoms in Cu_{62} was determined by

https://doi.org/10.1021/jacsau.5c00099
JACS Au 2025, 5, 1884−1893

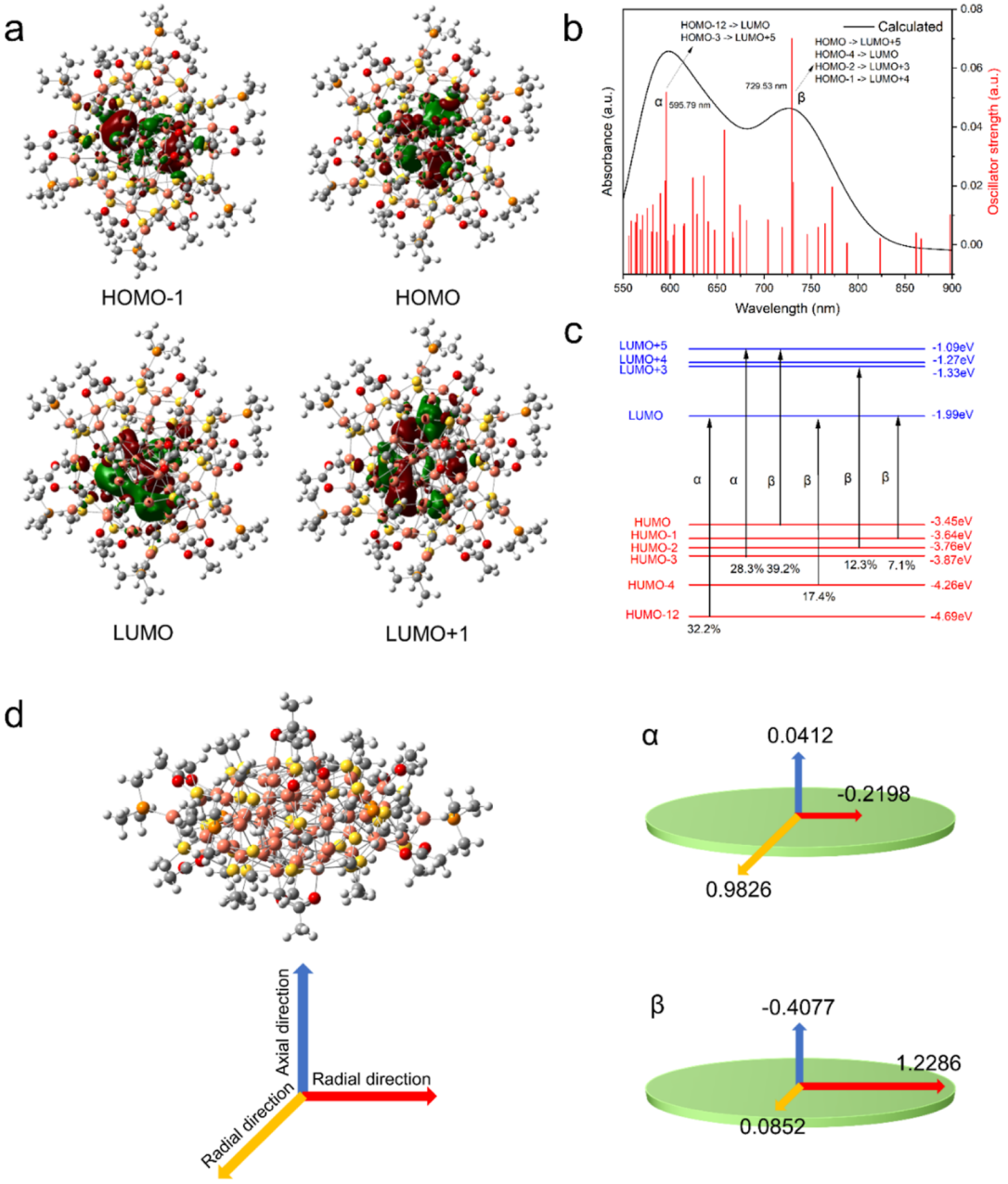

Figure 3. (a) Frontier molecular orbital of Cu_{62}. (b) Calculated UV−vis−NIR absorption spectra of Cu_{62}. (c) Kohn−Sham molecular energy level diagram. (d) Structure of Cu_{62} and schematic plot of transition electric dipole moments along radial and axial directions of Cu_{62}.

integrating the area under the peak corresponding to hydride atoms at 8.31 ppm, along with the characteristic peak at 6.10 ppm associated with the stoichiometric internal standard, 1, 3, 5-trimethoxybenzene (Figure S17). Based on these findings, it can be tentatively concluded that the Cu_{62} cluster consists of ten hydride atoms. The composition of Cu_{62} was further confirmed by thermogravimetric analysis (TGA) and elemental analysis (Figures S18 and S19). TGA profiles demonstrate the complete removal of nonmetallic components in Cu_{62} beyond 800 °C, resulting in a residual mass percentage (approximately 40%) that corresponds to the stoichiometric Cu proportion in the molecular formula. Elemental analysis results also demonstrate close agreement with the theoretical stoichiometric ratios. Therefore, the more plausible molecular formula for Cu_{62} is $[Cu_{62}(4\text{ F-PhS})_{30}(CF_3COO)_8(PPh_3)_6H_{10}]$.

We also employed a combinatorial methodology to determine the positions of the 10 hydride atoms within the Cu_{62} cluster. Through a thorough analysis of the crystal structure and utilization of data from previously characterized copper hydride clusters, we inferred the locations of the hydride atoms based on the residual peaks observed in the differential electron density map derived from the crystallographic data. Subsequently, the precise coordinates of these hydrides were refined using the least-squares optimization method. To enhance our understanding of the structure and stability of these configurations containing hydride, we conducted density functional theory (DFT) calculations (vide infra). As shown in Figure S20, the hydrides within the Cu_{62} cluster can be categorized into two distinct types based on their coordination modes and spatial arrangements. The first type comprises four hydrides located within the core of

https://doi.org/10.1021/jacsau.5c00099
JACS Au 2025, 5, 1884−1893

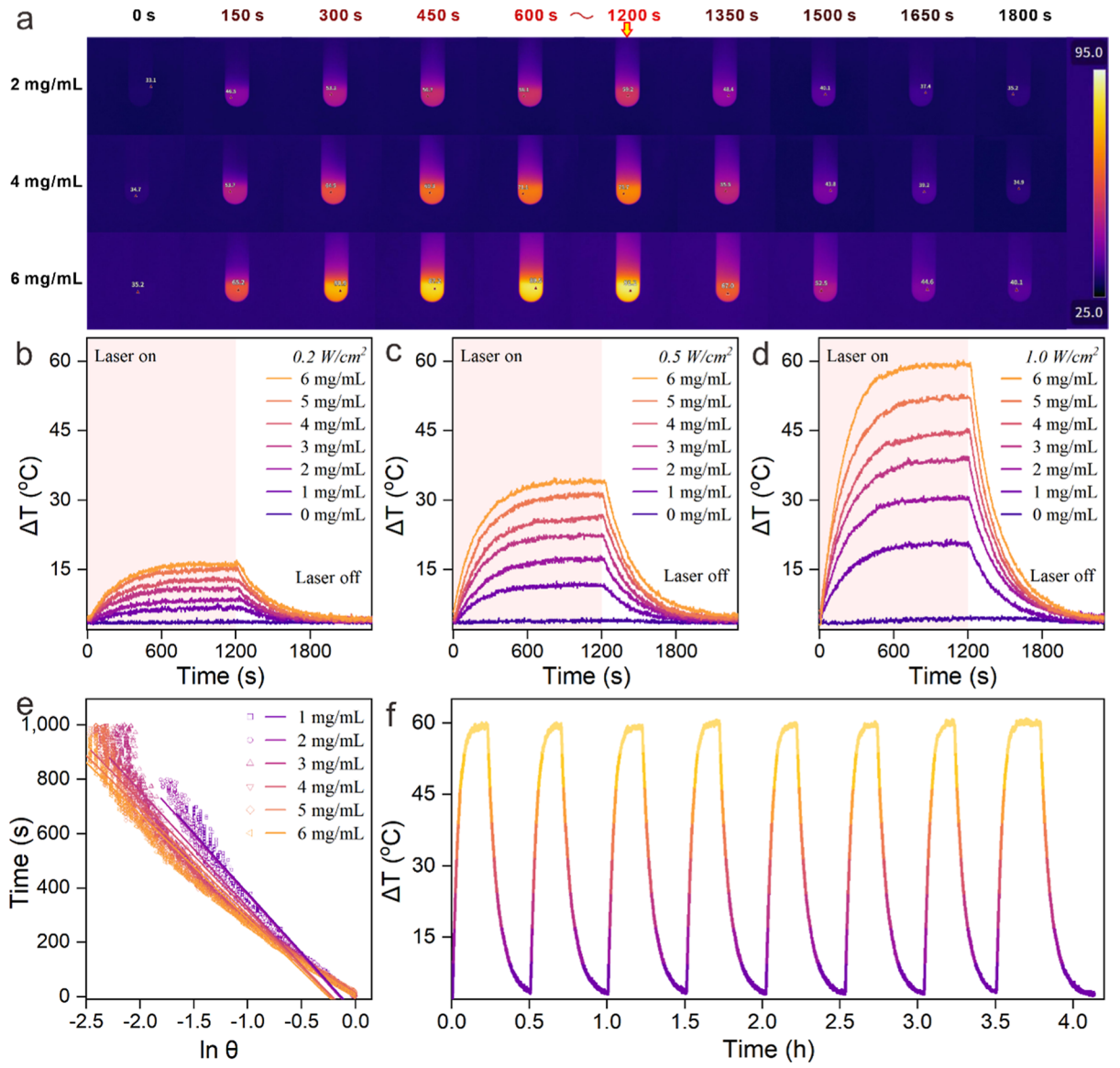

Figure 4. Photothermal conversion results. (a) IR thermal images recorded with a thermal imaging camera at different exposure times and concentrations. (b–d) Time-dependent photothermal curve of a Cu_{62} solution with different concentrations upon 808 nm laser irradiation at 0.2, 0.5, and 1.0 W/cm^2 laser intensity. (e) Linear relationship between time and ln θ. (f) Photothermal heating and natural cooling cycles under 808 nm laser irradiation at a power density of 1.0 W/cm^2.

the Cu_{62} cluster, while the second type consists of six hydrides positioned externally to the core. The coordination mode associated with these hydrides is designated as μ_3, and the average bond length between copper and hydride (Cu–H) is measured to be 1.738 Å.

The cyclic voltammetry (CV) data of Cu_{62} in CH_2Cl_2 are presented in Figure S21, illustrating the presence of an electrochemical bandgap of approximately 1.6 eV. This corresponds to the significant HOMO–LUMO gap calculated by DFT, which is 1.46 eV (vide infra). A solution of Cu_{62} in DMF exhibited an orange color (Figure S22, inset). Figure S22 displays the UV–vis–NIR spectra of Cu_{62} in DMF, revealing a prominent sharp peak at ~ 300 nm. Interestingly, a broad band was observed at ~760 nm. The linear relationship between the absorbance of the peak at 760 nm and the concentration of the cluster suggests that the presence of the peak is not attributed to other impurities (Figure S23). The wavelength of photons corresponding to an energy of 1.6 eV is 760 nm, which is also consistent with the absorption peak of Cu_{62} in the near-infrared region, as observed in the UV–vis–NIR spectrum.

To gain insights into the electronic structure and the origin of the NIR band of the cluster, we analyzed its molecular orbitals (MO) using density functional theory (DFT) calculations with the Gaussian 16 package (see the Computational Details in the Methods section). In order to reduce computational cost, we simplified the ligands from CF_3COO to CH_3COO, from PPh_3 to PMe_3, from *p*-FPh to Ph. It should be noted that this type of simplification has been deemed reasonable in previous studies. The structure of Cu_{62} was relaxed to its nearest local energy minimum based on X-ray single crystal analysis, and its main bond lengths were found to match well with the experimental data (Tables S2 and S3).

Figure 3a illustrates the distribution of the Frontier MO of the cluster. It is clear that the highest occupied molecular orbital (HOMO) and lowest unoccupied molecular orbital (LUMO) are predominantly localized around the copper (Cu)

https://doi.org/10.1021/jacsau.5c00099
JACS Au 2025, 5, 1884–1893

atoms. The frontier MO diagrams indicate that the cluster does not display any noticeable superatomic orbital characteristics (Figure S24).[56] Figure 3b displays the UV−vis−NIR absorption spectrum calculated via the TDDFT method. The primary simulated absorption peaks demonstrate a strong correlation with their corresponding experimental values. The peak (α transition), which is at 595.79 nm, is primarily attributed to the electronic transitions HOMO−12 → LUMO (32.2%) and HOMO−3 → LUMO + 5 (28.3%). The peak (β transition), which is at 729.53 nm in the near-infrared region, corresponds to the transitions HOMO → LUMO + 5 (39.2%), HOMO−4 → LUMO (17.4%), HOMO−2 → LUMO + 3 (12.3%), and HOMO−1 → LUMO + 4 (7.1%). Depicted in Figure 3c is the energy level diagram of the relevant Kohn−Sham orbitals, revealing a HOMO−LUMO gap of 1.46 eV, which agrees with the experimentally determined electrochemical bandgap. The large HOMO−LUMO gap suggests that Cu_{62} is electronically stable as a neutral species. Shown in Figure 3d is the schematic plot of the transition electric dipole moments along the radial and axial directions of the cluster. It is evident that the transition dipole moment along the x and y axes is considerably stronger than that along the z axis. Specifically, the transition electric dipole moment for both peaks α and β is maximized in the radial direction. Since the oscillator strength is proportional to the square of the transition dipole moment, it is suggested that the cluster exhibits a large oscillator strength.

Several recent studies have revealed that the high oscillator strength of gold or silver clusters in axial or radial directions enhances their photothermal conversion.[29,57] Therefore, it is believed that Cu_{62} demonstrates exceptional photothermal conversion properties. Photothermal conversion is a significant method for utilizing light energy, in which photothermal conversion materials initially absorb light energy and subsequently convert it into thermal energy for further utilization. Due to the advantages of weak tissue attenuation and minimal tissue damage offered by NIR lasers (wavelength range ~780−2500 nm), materials capable of utilizing NIR find wide application in the biomedical field, including photothermal therapy (PTT) and photoacoustic imaging (PA).[58−62] With its rare flat shape and certain absorption in the NIR range, we hypothesized that Cu_{62} is an excellent candidate for photothermal conversion. Considering the solubility of Cu_{62} and the boiling point of the solvent, DMF was selected as the optimal solvent for investigating the photothermal properties of Cu_{62} (Table S4). Therefore, we conducted an investigation into the photothermal performance of Cu_{62}. Prior to measurement, the cluster was dissolved in DMF in concentrations ranging from 0 to 6 mg/mL, and the photothermal conversion experiment was conducted at room temperature (~300 K) under NIR irradiation (808 nm laser with power densities of 0.2, 0.5, and 1.0 W/cm^2, respectively).

As shown in Figure 4a, the temperature of the Cu_{62} solution increased rapidly within 10 min and then reached a state of thermal equilibrium. The temperature of the solution gradually decreased to room temperature when the laser was turned off. Further analysis revealed a positive correlation between the highest temperatures and both the concentration and the optical power. Under an irradiation of 0.2 W/cm^2, the solutions with concentrations ranging from 1 to 6 mg/mL reached the highest temperature increase of 35.3, 36.4, 38.8, 40.9, 43.1, and 44.4 °C, respectively (Figure 4b). Similarly, under irradiation of 0.5 W/cm^2, the highest temperature gaps of 40.5, 46.3, 51.3, 55.4, 60.4, and 63.1 °C were obtained for the different concentrations (Figure 4c). The temperature could even be enhanced up to 50.8, 60.4, 68.7, 74.4, 82.0, and 90.3 °C for the solutions under irradiation of 1.0 W/cm^2 (Figure 4d). It is worth noting that the temperature of the blank group, in the absence of clusters, remained essentially unchanged under the irradiation of the 808 nm laser at all three light power densities. The aforementioned data demonstrate that Cu_{62} exhibits favorable photothermal conversion performance in the NIR light spectrum. By analyzing the cooling curve after 1.0 W/cm^2 laser irradiation in different concentrations (Figure 4e), it was calculated that the PCE of Cu_{62} is approximately 55.98% (Figure S25). This value exceeds that of most cluster-based materials documented in the literature (Table S5) and remains the highest in copper NCs, to the best of our knowledge. Finally, the stability of Cu_{62} during the process of photothermal conversion was assessed. No significant changes in the photothermal conversion properties of the Cu_{62} cluster solution were observed during eight and 30 heating−cooling cycles (with and without irradiation), as well as under continuous illumination for 14 h (Figures 4f and S26). Furthermore, the UV−vis spectra obtained before and after the cyclic testing were found to be almost identical (Figure S27).

The PCE of Cu_{62} further confirms that the radial oscillation of excitons in the oblate structure can provide a good photothermal performance, similar to the longitudinal plasmon resonance in metallic-state nanorods. Additionally, we also measured the photothermal conversion of other pure copper NCs with different shapes (Figure S28), including tetrahedral-shaped NCs ($Cu_8(S_2CN(CH_3)_2)_6(PPh_3)_4$ and $Cu_{29}(AdmS)_{12}(PPh_3)_4Cl_6H_{10}$), spherical-shaped NCs ($Cu_{20}Se(PhSe)_{12}(PPh_3)_2(C_6H_5COO)_6$ and $[SCu_{54}Cl_{12}(tBuS)_{20}(NO_3)_{12}]$), rod-shaped NCs $[Cu_{12}H_3(Tfdpf)_6(OAc)_2]\cdot OAc$ and $Cu_{18}H(PET)_{14}(TPP)_6(NCS)_3$, and dumbbell-shaped NCs ($Cu_{66}Cl_8(PPh_3)_8(SC_2H_5)_{32}H_{24}$).[63−68] Under the same conditions (6 mg/mL, 808 nm laser, 1.0 W/cm^2), the photothermal properties of NCs without high aspect ratios were significantly lower than those of the Cu_{62} cluster. Additionally, the NCs with high aspect ratios but smaller cores also exhibited inferior photothermal performance compared with the Cu_{62} cluster (Figure S29). This experimental result further demonstrates that the unique large core flat structure can effectively confine the radial occurrence of exciton transitions, thereby forming exciton oscillations similar to plasmon resonances, which provide a pathway for photothermal conversion. In summary, the characteristics of Cu_{62}, including its high PCE in the NIR region, absolute monodispersion, clear structure, and composition, make it highly promising for practical applications, such as photothermal therapy and solar-driven water evaporation.

3. CONCLUSIONS

In conclusion, a Cu nanocluster of $Cu_{62}(4\text{-}FPhS)_{30}(CF_3COO)_8(PPh_3)_6H_{10}$ was synthesized and studied. This nanocluster exhibits a rare flat oblate structure and shows near-infrared absorption. The molecular structure of the nanocluster reveals the stabilization of a flat windmill-shaped metal core by a ligand shell consisting of carboxylates, thiolates, and phosphines. The aspect ratio of the metal kernel of the cluster can reach up to 2.6, which is uncommon in the field of copper nanoclusters. Additionally, the cluster displays a near-infrared band at 760 nm, which is unprecedented for

https://doi.org/10.1021/jacsau.5c00099
JACS Au 2025, 5, 1884−1893

copper cluster materials. Density functional theory computations indicate that the near-infrared transitions of the cluster primarily occur at the equatorial radius of its metal core. The unique flat shape and near-infrared absorption of the Cu_{62} cluster also make it highly effective in photothermal conversion. When exposed to 808 nm light, the cluster can achieve a temperature increase from room temperature to approximately 90 °C within 10 min and demonstrate a high PCE of 55.98%. This performance surpasses that of other cluster-based photothermal conversion materials. This research not only presents an efficient strategy for shape control to enhance the performance of copper nanoclusters in photothermal conversion, but also highlights the significant potential of atomically precise copper nanoclusters in the field of material science.

4. METHODS SECTION

4.1. Materials

Copper(II) 2,2,2-trifluoroacetate hydrate ($Cu(OOCCF_3)_2{\cdot}H_2O$, 95%), 4-fluorothiophenol (4-FC_6H_4SH, 97%), and bis-(triphenylphosphino)-cuprous borohydride ($(PPh_3)_2CuBH_4$, 98%) were purchased from Bidepharm. (Shanghai, China). Chloroplatinic acid hexahydrate (ACS, Pt 37.5%) was purchased from Aladdin (Shanghai, China). Dichloromethane (CH_2Cl_2, A.R.), methanol (CH_3OH, A.R.), and ether ($C_4H_{10}O$, A.R.) were purchased from Sinopharm Chemical Reagent Co., Ltd. (Shanghai, China). All other reagents were used as received without further purification. The clusters Cu_8, Cu_{29}, Cu_{20}, Cu_{54}, and Cu_{66} were synthesized according to previous reports.[50,63−66]

4.2. Synthesis of Cu_{62}

$Cu(CF_3CO_2)_2{\cdot}H_2O$ (30.8 mg, 0.10 mmol) was fully dissolved in the mixed solvents of dichloromethane and methanol to make a clear blue solution. Then, a dichloromethane solution containing 4-fluorothiophenol (5.3 μL, 0.05 mmol) and bis(triphenylphosphino)-cuprous borohydride (40 mg) were successively added into the blue solution under vigorous stirring. The color of the solution turned form blue to pale orange and finally dark red. After the solution was stirred for 3 h, 1 mg of H_2PtCl_6 was added into the solution, followed by stirring for another 6 h. The solution was then centrifuged to remove any solid byproduct. Dark red block single crystals were obtained after diffusion of ether into the solution over 2 weeks. Cu_{62}-D was synthesized with the same method by using $(PPh_3)_2CuBD_4$ instead of $(PPh_3)_2CuBH_4$ as the reducing agent in the synthesis.

4.3. Characterizations

4.3.1. SC-XRD. The diffraction data of the single crystals were collected on an Agilent Technologies SuperNova system X-ray single-crystal diffractometer using Cu Kα (λ = 1.54184 Å) at 100 K. The data were processed using CrysAlis^{Pro} software. The structure was solved and refined using Full-matrix least-squares based on F^2 using ShelXT,[69] ShelXL[70] in Olex2.[71] Table S1 shows detailed crystal data and structural improvements for this compound. The CCDC 2386192 contains the supplementary crystallographic data for this paper. These data can be obtained free of charge from The Cambridge Crystallographic Data Centre.

4.3.2. Nuclear Magnetic Resonance. ^1H, ^2H, and ^{31}P NMR spectra were collected at ambient conditions on a Bruker AV-600 spectrometer with solvent residual signal as an internal reference. All data were processed on MestReNova software.

4.3.3. UV−Vis−NIR Absorption Spectroscopy. UV−Vis−NIR spectra were collected by a JASCOV-650 Spectrophotometer using a quartz cuvette of 1 mm path length. The signal from the blank solvent was subtracted.

4.3.4. Electrospray Ionization Mass Spectrometry. Mass spectra were collected using an agilent 6224 time-of-flight mass spectrophotometer. The dilute sample solutions were passed over oraganic filters (pore diameter: 0.22 μm) in advance. The typical conditions for experiments were set as capillary voltage: 4.0 kV, sample injection rate: 1.2 mL/h, drying gas temperature: 150 °C, nebulizer pressure: 0.2 MPa and drying gas flow rate: 4 L/h.

4.3.5. Energy-Dispersive X-ray Spectroscopy. EDS was carried out on a Bruker XFlash6100 at room temperature.

4.3.6. X-ray Photoelectron Spectroscopy. The XPS spectral data for the Cu_{62} cluster were tested on an ESCALAB Xi+. All spectra were corrected with the C 1s peak (284.5 eV).

4.3.7. Electrochemical Characterizations. The electrochemical properties of the cluster were studied by CV experiments. The electrochemical measurements were carried out on a CHI760E electrochemical workstation (Shanghai Chenhua Co., China) with a typical three-electrode system under a N_2 atmosphere at room temperature. During all measurements, the Pt wire and silver/silver chloride electrode (Ag/AgCl) served as the counter and reference electrodes, respectively. The working electrode was assembled by dropping 10 μL of homogeneous ink with a crystal cluster on a glassy carbon electrode and dried naturally. The geometric area of the working electrode was $\pi \times (0.15)^2$ cm^2, and the sample loading was 0.1 mg/cm^2. Moreover, the solvent/electrolyte system was used in a small glass cell containing 0.1 M $TBAPF_6$/DCM. For the CV experiments, the voltage range we used is −1.0 V−1.50 V (vs Ag/AgCl), and the scan rate is 0.1 V/s.

4.3.8. Computational Details. The density functional theory (DFT) and time-dependent density functional theory calculations for the Cu_{62} nanocluster were conducted by using the Gaussian 16 package. The PBE functional in combination with the def2-SV(P) basis set was employed for all calculations.[72,73] Frontier molecular orbital analysis was conducted using GaussView 6.0 software. Kohn−Sham orbital analysis was carried out with the Multiwfn 3.8 software.[74] To save computational cost, we simplified ligands from CF_3COO to CH_3COO, from PPh_3 to PMe_3, and from *p*-FPh to Ph.

4.3.9. Thermal Equipment. Photothermal measurements were conducted using a LASEVER808HX-8W-FC laser. The photothermal behavior of the sample was monitored by using the FOTRIC 246M-M50 infrared thermal imager test platform. Infrared photos and real-time temperatures were extracted from the video by AnalyzIR software.

Additionally, PCE calculations were performed as part of this study. Based on the total energy balance for this system

$$\sum_i m_i C_{p,i} \frac{dT}{dt} = Q_s - Q_{loss}$$

where m_i (0.948 g) and $C_{p,i}$ (2.14 J (g °C)$^{-1}$) are the mass and heat capacity of system components (*N*,*N*-dimethylformamide), respectively. T is the system temperature, and t is time. Q_s is the photothermal heat energy input by the laser (808 nm) to the sample. Q_{loss} is the thermal energy lost to the surroundings.

When the temperature is maximum, the system is in balance, $dT = 0$

$$Q_s = Q_{loss} = hS(T - T_{surr}) = hS(T_{max} - T_{surr}) = hS\Delta T_{max}$$

where h is the heat transfer coefficient, S is the surface area of the container, T_{surr} is the ambient temperature of the surroundings (~28 °C), T_{max} is the maximum system temperature, and ΔT_{max} is the maximum temperature change at the steady state (plateau).

The PCE η is calculated from the following equation

$$\eta = \frac{Q_s}{Q_I} = \frac{hS(T - T_{surr})}{I(1 - 10^{-A_\lambda})} = \frac{hS\Delta T_{max}}{I(1 - 10^{-A_\lambda})}$$

where Q_I is the photothermal energy absorbed by the sample when irradiated with laser (808 nm), I is the laser power (1.0 W/cm^2), and A_λ is the absorbance of the samples at the wavelength of λ (808 nm).

In order to obtain the hS, dimensionless driving force temperature θ and sample system time constant τ_s are introduced as follows

$$\theta = \frac{T - T_{surr}}{T_{max} - T_{surr}}$$

https://doi.org/10.1021/jacsau.5c00099
JACS Au 2025, 5, 1884−1893

and

$$\tau_s = \frac{\sum_i m_i C_{p,i}}{hS}$$

thus

$$\begin{aligned}\frac{d\theta}{dt} &= \frac{1}{T_{max} - T_{surr}}\frac{dT}{dt} \\ &= \frac{1}{\Delta T_{max}}\frac{Q_s - Q_{loss}}{\sum_i m_i C_{p,i}} \\ &= \frac{Q_s}{\tau_s hS\Delta T_{max}} - \frac{Q_{loss}}{\tau_s hS\Delta T_{max}} \\ &= \frac{1}{\tau_s}\frac{Q_s}{hS\Delta T_{max}} - \frac{hS(T - T_{surr})}{\tau_s hS(T_{max} - T_{surr})} \\ &= \frac{1}{\tau_s}\frac{Q_s}{hS\Delta T_{max}} - \frac{\theta}{\tau_s}\end{aligned}$$

When the laser is off (after the system reaches the maximum temperature), $Q_s = 0$. Therefore

$$\frac{d\theta}{dt} = \frac{1}{\tau_s}\frac{Q_s}{hS\Delta T_{max}} - \frac{\theta}{\tau_s} = -\frac{\theta}{\tau_s}$$

and

$$t = -\tau_s \ln \theta$$

To sum up, the value of τ_s can be obtained from the slope of the cooling time vs ln θ plot, and $hS = \frac{1}{\tau_s}\sum_i m_i C_{p,i}$

■ ASSOCIATED CONTENT

Supporting Information

The Supporting Information is available free of charge at https://pubs.acs.org/doi/10.1021/jacsau.5c00099.

Crystallographic data (CIF)

Additional characterization data (digital photographs, structural information, experimental UV−vis−NIR spectra, EDS images, NMR data, XPS analysis, CV curve, DFT calculations, and photothermal conversion of other clusters) (PDF)

■ AUTHOR INFORMATION

Corresponding Authors

Song Wang − *Key Laboratory of Precision and Intelligent Chemistry, School of Chemistry and Materials Science, University of Science and Technology of China, Hefei, Anhui 230026, China;* orcid.org/0000-0003-1252-8091; Email: wsong09@ustc.edu.cn

Hui Shen − *College of Energy Materials and Chemistry, Inner Mongolia University, Hohhot 010021, China;* orcid.org/0000-0003-4800-437X; Email: shen@imu.edu.cn

Authors

Bingzheng Yan − *College of Energy Materials and Chemistry, Inner Mongolia University, Hohhot 010021, China; School of Physical Science and Technology, Inner Mongolia University, Hohhot 010021, China*

Jing Sun − *College of Energy Materials and Chemistry, Inner Mongolia University, Hohhot 010021, China*

Jiahe Liu − *Key Laboratory of Precision and Intelligent Chemistry, School of Chemistry and Materials Science, University of Science and Technology of China, Hefei, Anhui 230026, China*

Lei Li − *New Cornerstone Science Laboratory, State Key Laboratory for Physical Chemistry of Solid Surfaces, Collaborative Innovation Center of Chemistry for Energy Materials, and National & Local Joint Engineering Research Center of Preparation Technology of Nanomaterials, College of Chemistry and Chemical Engineering, Xiamen University, Xiamen 361005, China*

Hongwen Deng − *New Cornerstone Science Laboratory, State Key Laboratory for Physical Chemistry of Solid Surfaces, Collaborative Innovation Center of Chemistry for Energy Materials, and National & Local Joint Engineering Research Center of Preparation Technology of Nanomaterials, College of Chemistry and Chemical Engineering, Xiamen University, Xiamen 361005, China*

Qinghua Xu − *College of Energy Materials and Chemistry, Inner Mongolia University, Hohhot 010021, China;* orcid.org/0009-0009-8638-4474

Complete contact information is available at: https://pubs.acs.org/10.1021/jacsau.5c00099

Author Contributions

⊥B.Y., J.S., and J.L. contributed equally to this work.

Notes

The authors declare no competing financial interest.

■ ACKNOWLEDGMENTS

H.S. acknowledges the financial support from the National Natural Science Foundation of China (22301149), National Key R&D Program of China (2023YFB3507100), Program for Young Talents of Science and Technology in Universities of Inner Mongolia Autonomous Region (NJYT23035), and start-up funding of Inner Mongolia University (10000-23112101/043). S.W. acknowledges the National Natural Science Foundation of China (Grant No. 22203082) for financial support.

■ REFERENCES

(1) Chakraborty, I.; Pradeep, T. Atomically Precise Clusters of Noble Metals: Emerging Link between Atoms and Nanoparticles. *Chem. Rev.* **2017**, *117*, 8208−8271.

(2) Jin, R.; Zeng, C.; Zhou, M.; Chen, Y. Atomically Precise Colloidal Metal Nanoclusters and Nanoparticles: Fundamentals and Opportunities. *Chem. Rev.* **2016**, *116*, 10346−10413.

(3) Matus, M.; Häkkinen, H. Understanding ligand-protected noble metal nanoclusters at work. *Nat. Rev. Mater.* **2023**, *8*, 372−389.

(4) Takano, S.; Tsukuda, T. Chemically Modified Gold/Silver Superatoms as Artificial Elements at Nanoscale: Design Principles and Synthesis Challenges. *J. Am. Chem. Soc.* **2021**, *143*, 1683−1698.

(5) Lim, D. C.; Seo, B. Y.; Nho, S. G.; Kim, D. H.; Hong, E. M.; Lee, J. Y.; Park, S. Y.; Lee, C. L.; Kim, Y. D.; Cho, S. Emissive Nanoclusters Based on Subnanometer-Sized Au_{38} Cores for Boosting the Performance of Inverted Organic Photovoltaic Cells. *Adv. Energy Mater.* **2015**, *5*, 1500393.

(6) Isozaki, K.; Ueno, R.; Ishibashi, K.; Nakano, G.; Yin, H. Z.; Iseri, K.; Sakamoto, M.; Takaya, H.; Teranishi, T.; Nakamura, M. Gold Nanocluster Functionalized with Peptide Dendron Thiolates: Acceleration of the Photocatalytic Oxidation of an Amino Alcohol in a Supramolecular Reaction Field. *ACS Catal.* **2021**, *11*, 13180−13187.

(7) Dong, C.; Song, X.; Hasanov, B. E.; Yuan, Y.; Gutierrez-Arzaluz, L.; Yuan, P.; Nematulloev, S.; Bayindir, M.; Mohammed, O. F.; Bakr, O. M. Organic-Inorganic Hybrid Glasses of Atomically Precise Nanoclusters. *J. Am. Chem. Soc.* **2024**, *146*, 7373−7385.

(8) Jordan, A. J.; Lalic, G.; Sadighi, J. P. Coinage Metal Hydrides: Synthesis, Characterization, and Reactivity. *Chem. Rev.* **2016**, *116*, 8318−8372.
(9) Li, Q.; Kulikowski, J.; Doan, D.; Tertuliano, O. A.; Zeman, C. J.; Wang, M. M.; Schatz, G. C.; Gu, X. W. Mechanical nanolattices printed using nanocluster-based photoresists. *Science* **2022**, *378*, 768−773.
(10) Li, Y.; Zhou, M.; Song, Y.; Higaki, T.; Wang, H.; Jin, R. Double-helical assembly of heterodimeric nanoclusters into supercrystals. *Nature* **2021**, *594*, 380.
(11) Shi, W.; Zeng, L.; He, R.; Han, X.; Guan, Z.; Zhou, M.; Wang, Q. Near-unity NIR phosphorescent quantum yield from a room-temperature solvated metal nanocluster. *Science* **2024**, *383*, 326−330.
(12) Wang, X.; Yin, B.; Jiang, L.; Yang, C.; Liu, Y.; Zou, G.; Chen, S.; Zhu, M. Ligand-protected metal nanoclusters as low-loss, highly polarized emitters for optical waveguides. *Science* **2023**, *381*, 784−790.
(13) Zhang, Y.; He, S. R.; Yang, Y.; Zhang, T. S.; Zhu, Z. M.; Fei, W. W.; Li, M. B. Preorganized Nitrogen Sites for Au_{11} Amidation: A Generalizable Strategy toward Precision Functionalization of Metal Nanoclusters. *J. Am. Chem. Soc.* **2023**, *145*, 12164−12172.
(14) Arima, D.; Mitsui, M. Structurally Flexible Au−Cu Alloy Nanoclusters Enabling Efficient Triplet Sensitization and Photon Upconversion. *J. Am. Chem. Soc.* **2023**, *145*, 6994−7004.
(15) Yi, H.; Han, S. M.; Song, S.; Kim, M.; Sim, E.; Lee, D. Superatom-in-Superatom $[RhH@Ag_{24}(SPhMe_2)_{18}]^{2-}$ Nanocluster. *Angew. Chem., Int. Ed.* **2021**, *60*, 22293−22300.
(16) Yoskamtorn, T.; Yamazoe, S.; Takahata, R.; Nishigaki, J.; Thivasasith, A.; Limtrakul, J.; Tsukuda, T. Thiolate-Mediated Selectivity Control in Aerobic Alcohol Oxidation by Porous Carbon-Supported Au_{25} Clusters. *ACS Catal.* **2014**, *4*, 3696−3700.
(17) Tang, L.; Ma, A.; Zhang, C. M.; Liu, X. G.; Jin, R. C.; Wang, S. X. Total Structure of Bimetallic Core−Shell $[Au_{42}Cd_{40}(SR)_{52}]^{2-}$ Nanocluster and Its Implications. *Angew. Chem., Int. Ed.* **2021**, *60*, 17969−17973.
(18) Chiu, T. H.; Liao, J. H.; Wu, Y. Y.; Chen, J. Y.; Chen, Y. J.; Wang, X. P.; Kahlal, S.; Saillard, J. Y.; Liu, C. W. Hydride Doping Effects on the Structure and Properties of Eight-Electron Rh/Ag Superatoms: The $[RhH_x@Ag_{21-x}\{S_2P(O^nPr)_2\}_{12}]$ (x = 0−2) Series. *J. Am. Chem. Soc.* **2023**, *145*, 16739−16747.
(19) Wang, Y.; Liu, X. H.; Wang, Q. K.; Quick, M.; Kovalenko, S. A.; Chen, Q. Y.; Koch, N.; Pinna, N. Insights into Charge Transfer at an Atomically Precise Nanocluster/Semiconductor Interface. *Angew. Chem., Int. Ed.* **2020**, *59*, 7748−7754.
(20) Narouz, M. R.; Osten, K. M.; Unsworth, P. J.; Man, R. W. Y.; Salorinne, K.; Takano, S.; Tomihara, R.; Kaappa, S.; Malola, S.; Dinh, C. T.; Padmos, J. D.; Ayoo, K.; Garrett, P. J.; Nambo, M.; Horton, J. H.; Sargent, E. H.; Häkkinen, H.; Tsukuda, T.; Crudden, C. M. N-heterocyclic carbene-functionalized magic-number gold nanoclusters. *Nat. Chem.* **2019**, *11*, 419−425.
(21) Kim, H.; Yoo, T.; Bootharaju, M. S.; Kim, J.; Chung, D. Y.; Hyeon, T. Noble Metal-Based Multimetallic Nanoparticles for Electrocatalytic Applications. *Adv. Sci.* **2022**, *9*, 2104054.
(22) Han, B.; Liu, Z.; Feng, L.; Wang, Z.; Gupta, R. K.; Aikens, C. M.; Tung, C.; Sun, D. Polymorphism in Atomically Precise Cu_{23} Nanocluster Incorporating Tetrahedral $[Cu_4]^0$ Kernel. *J. Am. Chem. Soc.* **2020**, *142*, 5834−5841.
(23) Kenzler, S.; Schrenk, C.; Schnepf, A. $Au_{108}S_{24}(PPh_3)_{16}$: A Highly Symmetric Nanoscale Gold Cluster Confirms the General Concept of Metalloid Clusters. *Angew. Chem., Int. Ed.* **2017**, *56*, 393−396.
(24) Qu, M.; Li, H.; Xie, L.; Yan, S.; Li, J.; Wang, J.; Wei, C.; Wu, Y.; Zhang, X. Bidentate Phosphine-Assisted Synthesis of an All-Alkynyl-Protected Ag_{74} Nanocluster. *J. Am. Chem. Soc.* **2017**, *139*, 12346−12349.
(25) Si, W.; Zhang, C.; Zhou, M.; Tian, W.; Wang, Z.; Hu, Q.; Song, K.; Feng, L.; Huang, X.; Gao, Z.; Tung, C.; Sun, D. Two triplet emitting states in one emitter: Near-infrared dual-phosphorescent Au_{20} nanocluster. *Sci. Adv.* **2023**, *9*, No. eadg3587.
(26) Guan, Z.; Zeng, J.; Nan, Z.; Wan, X.; Lin, Y.; Wang, Q. Thiacalix[4]arene: New protection for metal nanoclusters. *Sci. Adv.* **2016**, *2*, No. e1600323.
(27) Chen, T.; Lin, H.; Cao, Y.; Yao, Q.; Xie, J. Interactions of Metal Nanoclusters with Light: Fundamentals and Applications. *Adv. Mater.* **2022**, *34*, 2103918.
(28) Murphy, C. J.; Chang, H.; Falagan-Lotsch, P.; Gole, M. T.; Hofmann, D. M.; Hoang, K. N. L.; McClain, S. M.; Meyer, S. M.; Turner, J. G.; Unnikrishnan, M.; Wu, M.; Zhang, X.; Zhang, Y. Virus-Sized Gold Nanorods: Plasmonic Particles for Biology. *Acc. Chem. Res.* **2019**, *52*, 2124−2135.
(29) Fang, L.; Fan, W.; Bian, G.; Wang, R.; You, Q.; Gu, W.; Xia, N.; Liao, L.; Li, J.; Deng, H.; Yan, N.; Wu, Z. Sandwich-Kernelled AgCu Nanoclusters with Golden Ratio Geometry and Promising Photothermal Efficiency. *Angew. Chem., Int. Ed.* **2023**, *62*, No. e202305604.
(30) Huang, R. W.; Yin, J.; Dong, C.; Ghosh, A.; Alhilaly, M. J.; Dong, X.; Hedhili, M. N.; Abou-Hamad, E.; Alamer, B.; Nematulloev, S.; Han, Y.; Mohammed, O. F.; Bakr, O. M. $[Cu_{81}(PhS)_{46}(^tBuNH_2)_{10}(H)_{32}]^{3+}$ Reveals the Coexistence of Large Planar Cores and Hemispherical Shells in High-Nuclearity Copper Nanoclusters. *J. Am. Chem. Soc.* **2020**, *142*, 8696−8705.
(31) Deng, G.; Lee, K.; Deng, H.; Malola, S.; Bootharaju, M. S.; Hakkinen, H.; Zheng, N. F.; Hyeon, T. Alkynyl-Protected Chiral Bimetallic $Ag_{22}Cu_7$ Superatom with Multiple Chirality Origins. *Angew. Chem., Int. Ed.* **2023**, *62*, No. e202217483.
(32) Liu, X. G.; Ruiz, J.; Astruc, D. Prevention of aerobic oxidation of copper nanoparticles by anti-galvanic alloying: gold versus silver. *Chem. Commun.* **2017**, *53*, 11134−11137.
(33) Ma, X.; Si, Y.; Luo, L.; Wang, Z.; Zang, S. Q.; Mak, T. C. W. Directional Doping and Cocrystallizing an Open-Shell Ag_{39} Superatom via Precursor Engineering. *ACS Nano* **2022**, *16*, 5507−5514.
(34) Yang, S.; Chai, J.; Chong, H.; Song, Y.; Yu, H.; Zhu, M. Sulfonate, sulfide and thiolate ligands into an ultrasmall nanocluster: $[Ag_{40.13}Cu_{13.87}S_{19}(^tBuS)_{20}(^tBuSO_3)_{12}]$. *Chem. Commun.* **2018**, *54*, 4314−4316.
(35) Xu, X. X.; Liu, Y.; Sun, F.; Jia, Y. Y.; Xu, Q. H.; Tang, J. Q.; Xie, Z. L.; Sun, J.; Li, S. M.; Tang, Q.; Guo, S.; Shen, H.; Zheng, N. F. Array-Based Clusters of Copper with Largely Exposed Metal Sites for Promoting Catalysis. *Chem. Mater.* **2023**, *35*, 7588−7596.
(36) Wang, Y. M.; Lin, X. C.; Mo, K. M.; Xie, M.; Huang, Y. L.; Ning, G. H.; Li, D. An Atomically Precise Pyrazolate-Protected Copper Nanocluster Exhibiting Exceptional Stability and Catalytic Activity. *Angew. Chem., Int. Ed.* **2023**, *62*, No. e202218369.
(37) Nguyen, T. D.; Jones, Z. R.; Goldsmith, B. R.; Buratto, W. R.; Wu, G.; Scott, S. L.; Hayton, T. W. A Cu_{25} Nanocluster with Partial Cu(0) Character. *J. Am. Chem. Soc.* **2015**, *137*, 13319−13324.
(38) Dong, C.; Huang, R. W.; Chen, C.; Chen, J.; Nematulloev, S.; Guo, X.; Ghosh, A.; Alamer, B.; Hedhili, M. N.; Isimjan, T. T.; Han, Y.; Mohammed, O. F.; Bakr, O. M. $[Cu_{36}H_{10}(PET)_{24}(PPh_3)_6Cl_2]$ Reveals Surface Vacancy Defects in Ligand-Stabilized Metal Nanoclusters. *J. Am. Chem. Soc.* **2021**, *143*, 11026−11035.
(39) Xu, C.; Jin, Y. H.; Fang, H.; Zheng, H. J.; Carozza, J. C.; Pan, Y. X.; Wei, P. J.; Zhang, Z. Y.; Wei, Z.; Zhou, Z.; Han, H. X. A High-Nuclearity Copper Sulfide Nanocluster $[S\text{-}Cu_{50}]$ Featuring a Double-Shell Structure Configuration with Cu(II)/Cu(I) Valences. *J. Am. Chem. Soc.* **2023**, *145*, 25673−25685.
(40) Tang, Q.; Lee, Y.; Li, D. Y.; Choi, W.; Liu, C. W.; Lee, D.; Jiang, D. Lattice-Hydride Mechanism in Electrocatalytic CO_2 Reduction by Structurally Precise Copper-Hydride Nanoclusters. *J. Am. Chem. Soc.* **2017**, *139*, 9728−9736.
(41) Sharma, S.; Chakrahari, K. K.; Saillard, J.; Liu, C. W. Structurally Precise Dichalcogenolate-Protected Copper and Silver Superatomic Nanoclusters and Their Alloys. *Acc. Chem. Res.* **2018**, *51*, 2475−2483.
(42) Yang, G.; Xie, Y.; Wang, Y.; Tang, Y.; Chng, L. L.; Jiang, F.; Du, F.; Zhou, X.; Ying, J. Y.; Yuan, X. Water-soluble Cu_{30} nanoclusters as a click chemistry catalyst for living cell labeling via azide-alkyne cycloaddition. *Nano Res.* **2023**, *16*, 1748−1754.

https://doi.org/10.1021/jacsau.5c00099
JACS Au 2025, 5, 1884−1893

(43) Biswas, S.; Das, S.; Negishi, Y. Advances in Cu nanocluster catalyst design: recent progress and promising applications. *Nanoscale Horiz.* **2023**, *8*, 1509−1522.
(44) Liu, L.; Wang, Z.; Wang, Z.; Wang, R.; Zang, S. Q.; Mak, T. C. W. Mediating CO_2 Electroreduction Activity and Selectivity over Atomically Precise Copper Clusters. *Angew. Chem., Int. Ed.* **2022**, *61*, No. e202205626.
(45) Wang, L.; Yan, X.; Tian, G.; Xie, Z.; Shi, S.; Zhang, Y.; Li, S.; Sun, X.; Sun, J.; He, J.; Shen, H. Chiral copper-hydride nanoclusters: synthesis, structure, and assembly. *Dalton Trans.* **2023**, *52*, 3371−3377.
(46) Dhayal, R. S.; Liao, J.; Kahlal, S.; Wang, X.; Liu, Y.; Chiang, M.; van Zyl, W. E.; Saillard, J.; Liu, C. W. $[Cu_{32}(H)_{20}\{S_2P(O^iPr)_2\}_{12}]$: The Largest Number of Hydrides Recorded in a Molecular Nanocluster by Neutron Diffraction. *Chem. Eur. J.* **2015**, *21*, 8369−8374.
(47) Alamer, B.; Sagadevan, A.; Bodiuzzaman, M.; Murugesan, K.; Alsharif, S.; Huang, R. W.; Ghosh, A.; Naveen, M. H.; Dong, C.; Nematulloev, S.; Yin, J.; Shkurenko, A.; Abulikemu, M.; Dong, X.; Han, Y.; Eddaoudi, M.; Rueping, M.; Bakr, O. M. Planar Core and Macrocyclic Shell Stabilized Atomically Precise Copper Nanocluster Catalyst for Efficient Hydroboration of C−C Multiple Bond. *J. Am. Chem. Soc.* **2024**, *146*, 16295−16305.
(48) Ge, X.; Zeng, S. H.; Deng, H. G.; Teo, B. K.; Sun, C. F. Atom-precise copper nanoclusters based on FCC, BCC, and HCP structures. *Coord. Chem. Rev.* **2024**, *503*, 215667.
(49) Baghdasaryan, A.; Bürgi, T. Copper nanoclusters: designed synthesis, structural diversity, and multiplatform applications. *Nanoscale* **2021**, *13*, 6283−6340.
(50) Yan, B.; You, X.; Tang, X.; Sun, J.; Xu, Q.; Wang, L.; Guan, Z.; Li, F.; Shen, H. Carboxylate-Protected "Isostructural" Cu_{20} Nanoclusters as a Model System: Carboxylate Effect on Controlling Catalysis. *Chem. Mater.* **2024**, *36*, 1004−1012.
(51) Gao, Y.; Sun, X.; Tang, X.; Xie, Z.; Tian, G.; Nan, Z.; Yang, H.; Shen, H. An alkynyl-protected $Ag_{13-x}Cu_{6+x}$ nanocluster for catalytic hydrogenation. *Dalton Trans.* **2022**, *52*, 52−57.
(52) Shen, H.; Han, Y.; Wu, Q.; Peng, J.; Teo, B. K.; Zheng, N. F. Simple and Selective Synthesis of Copper-Containing Metal Nanoclusters Using $(PPh_3)_2CuBH_4$ as Reducing Agent. *Small Methods* **2021**, *5*, 2000603.
(53) Li, S.; Wu, Q.; You, X.; Ren, X.; Du, P.; Li, F.; Zheng, N. F.; Shen, H. Anchoring Frustrated Lewis Pair Active Sites on Copper Nanoclusters for Regioselective Hydrogenation. *J. Am. Chem. Soc.* **2024**, *146*, 27852−27860.
(54) Sun, J.; Tang, X. K.; Liu, Z. H.; Xie, Z. L.; Yan, B. Z.; Yin, R. F.; Chaolumen, C.; Zhang, J.; Fang, W. H.; Wei, J. Y.; Shen, H. Labile Ligands Protected Cu_{50} Nanoclusters with Tailorable Optical Limiting Effect. *ACS Mater. Lett.* **2024**, *6*, 281−289.
(55) Yonesato, K.; Yamazoe, S.; Yokogawa, D.; Yamaguchi, K.; Suzuki, K. A Molecular Hybrid of an Atomically Precise Silver Nanocluster and Polyoxometalates for H_2 Cleavage into Protons and Electrons. *Angew. Chem., Int. Ed.* **2021**, *60*, 16994−16998.
(56) Walter, M.; Akola, J.; Lopez-Acevedo, O.; Jadzinsky, P. D.; Calero, G.; Ackerson, C. J.; Whetten, R. L.; Grönbeck, H.; Häkkinen, H. A unified view of ligand-protected gold clusters as superatom complexes. *Proc. Natl. Acad. Sci. U.S.A.* **2008**, *105*, 9157−9162.
(57) Li, Y.; Song, Y.; Zhang, X.; Liu, T.; Xu, T.; Wang, H.; Jiang, D.; Jin, R. Atomically Precise Au_{42} Nanorods with Longitudinal Excitons for an Intense Photothermal Effect. *J. Am. Chem. Soc.* **2022**, *144*, 12381−12389.
(58) Li, J.; Yang, D.; Lyu, W.; Yuan, Y.; Han, X.; Yue, W.; Jiang, J.; Xiao, Y.; Fang, Z.; Lu, X.; Wang, W.; Huang, W. A Bioinspired Photosensitizer Performs Tumor Thermoresistance Reversion to Optimize the Atraumatic Mild-Hyperthermia Photothermal Therapy for Breast Cancer. *Adv. Mater.* **2024**, *36*, 2405890.
(59) Li, X.; Lovell, J. F.; Yoon, J.; Chen, X. Clinical development and potential of photothermal and photodynamic therapies for cancer. *Nat. Rev. Clin. Oncol.* **2020**, *17*, 657−674.
(60) Nam, J.; Son, S.; Park, K. S.; Zou, W.; Shea, L. D.; Moon, J. J. Cancer nanomedicine for combination cancer immunotherapy. *Nat. Rev. Mater.* **2019**, *4*, 398−414.
(61) Pan, Y.; Cheng, J.; Zhu, Y.; Zhang, J.; Fan, W.; Chen, X. Immunological nanomaterials to combat cancer metastasis. *Chem. Soc. Rev.* **2024**, *53*, 6399−6444.
(62) Yang, G.; Pan, X.; Feng, W.; Yao, Q.; Jiang, F.; Du, F.; Zhou, X.; Xie, J.; Yuan, X. Engineering Au_{44} Nanoclusters for NIR-II Luminescence Imaging-Guided Photoactivatable Cancer Immunotherapy. *ACS Nano* **2023**, *17*, 15605−15614.
(63) Sun, X.; Wang, Y.; Wu, Q.; Han, Y.; Gong, X.; Tang, X.; Aikens, C.; Shen, H.; Zheng, N. Cu_{66} nanoclusters from hierarchical square motifs: Synthesis, assembly, and catalysis. *Aggregate* **2024**, *6*, No. e651.
(64) Sun, J.; Yan, X.; Wang, L.; Xie, Z.; Tian, G.; Wang, L.; He, A.; Li, S.; Guo, Q.; Chaolumen; He, J.; Shen, H. Decorating an Anticuboctahedral Copper Kernel with Labile Surface Coatings for Controlling Optical and Catalytic Properties. *Inorg. Chem.* **2023**, *62*, 9005−9013.
(65) Sun, X.; Yan, B.; Gong, X.; Xu, Q.; Guo, Q.; Shen, H. Eight-Electron Copper Nanoclusters for Photothermal Conversion. *Chem. Eur. J.* **2024**, *30*, No. e202400527.
(66) Meng, X.; He, A.; Yan, X.; Wang, L.; Zhao, Z.; Jia, Y.; He, J.; Guo, S.; Shen, H. One-pot gram-scale synthesis of robust copper nanoclusters for photocatalytic difluoroalkylarylation of alkenes. *Polyoxometalates* **2025**, *4*, 9140080.
(67) Dong, G.; Pan, Z.; Han, B.; Tao, Y.; Chen, X.; Luo, G.; Sun, P.; Sun, C.; Sun, D. Multi-layer 3D Chirality and Double-Helical Assembly in a Copper Nanocluster with a Triple-Helical Cu_{15} Core. *Angew. Chem., Int. Ed.* **2023**, *62*, No. e202302595.
(68) Liu, C.; Yuan, S.; Wang, S.; Guan, Z.; Jiang, D.; Wang, Q. Structural transformation and catalytic hydrogenation activity of amidinate-protected copper hydride clusters. *Nat. Commun.* **2022**, *13*, 2082.
(69) Granlund, L.; Billinge, S. J.; Duxbury, P. M. Algorithm for systematic peak extraction from atomic pair distribution functions. *Acta Crystallogr., Sect. A:Found. Adv.* **2015**, *71*, 392−409.
(70) Sheldrick, G. M. A short history of SHELX. *Acta Crystallogr., Sect. A:Found. Adv.* **2008**, *64*, 112−122.
(71) Dolomanov, O. V.; Bourhis, L. J.; Gildea, R. J.; Howard, J. A. K.; Puschmann, H. OLEX2: a complete structure solution, refinement and analysis program. *J. Appl. Crystallogr.* **2009**, *42*, 339−341.
(72) Perdew, J. P.; Burke, K.; Ernzerhof, M. Generalized Gradient Approximation Made Simple. *Phys. Rev. Lett.* **1996**, *77*, 3865−3868.
(73) Weigend, F.; Ahlrichs, R. Balanced basis sets of split valence, triple zeta valence and quadruple zeta valence quality for H to Rn: Design and assessment of accuracy. *Phys. Chem. Chem. Phys.* **2005**, *7*, 3297−3305.
(74) Lu, T.; Chen, F. Multiwfn: A multifunctional wavefunction analyzer. *J. Comput. Chem.* **2012**, *33*, 580−592.

https://doi.org/10.1021/jacsau.5c00099
JACS Au 2025, 5, 1884−1893